APL Materials

RESEARCH ARTICLE | JULY 08 2026

Molecular beam epitaxy of wafer-scale O-band InAs/InGaAs quantum dots on GaAs for quantum photonics

Pavel S. Avdienko ; Lukas Hanschke ; Quirin Buchinger ; Nikolai Bart; Hubert Riedl ; Bianca Scaparra; Yu Xia; Ziria Herdegen ; Knut Müller-Caspary ; Gregor Koblmüller ; Tobias Huber-Loyola ; Arne Ludwig ; Andreas Pfenning ; Sven Höfling ; Kai Müller ; Jonathan J. Finley

APL Mater. 14, 071107 (2026)
https://doi.org/10.1063/5.0327103

Molecular beam epitaxy of wafer-scale O-band InAs/InGaAs quantum dots on GaAs for quantum photonics

Cite as: APL Mater. 14, 071107 (2026); doi: 10.1063/5.0327103
Submitted: 10 February 2026 • Accepted: 18 June 2026 •
Published Online: 8 July 2026

Pavel S. Avdienko,[1,a] Lukas Hanschke,[2] Quirin Buchinger,[3,4] Nikolai Bart,[5] Hubert Riedl,[1] Bianca Scaparra,[2] Yu Xia,[6] Ziria Herdegen,[6] Knut Müller-Caspary,[6] Gregor Koblmüller,[1,7] Tobias Huber-Loyola,[3,4,8] Arne Ludwig,[5] Andreas Pfenning,[3,4] Sven Höfling,[3] Kai Müller,[2] and Jonathan J. Finley[1,b]

AFFILIATIONS

[1] Walter Schottky Institute, Physics Department, School of Natural Sciences, Technical University of Munich, Am Coulombwall 4, 85748 Garching, Germany
[2] TUM School of Computation, Information and Technology, Technical University of Munich, 80333 Munich, Germany
[3] Julius-Maximilians-Universität Würzburg, Physikalisches Institut, Lehrstuhl für Technische Physik, Am Hubland, 97074 Würzburg, Germany
[4] Saqura Technologies GmbH, Paradiesstr. 15, 97855 Homburg am Main, Germany
[5] Ruhr University Bochum, Faculty of Physics and Astronomy, Experimental Physics VI, Universitätsstraße 150, 44801 Bochum, Germany
[6] Department of Chemistry and Center for NanoScience, Ludwig-Maximilians-University Munich, 81377 Munich, Germany
[7] Institute of Physics and Astronomy, Technical University of Berlin, Hardenbergstrasse 36, 10623 Berlin, Germany
[8] Karlsruhe Institute of Technology, Institute of Photonics and Quantum Electronics IQST, Engesserstr. 5, 76131 Karlsruhe, Germany

[a] **Author to whom correspondence should be addressed:** pavel.avdienko@tum.de
[b] jj.finley@tum.de

ABSTRACT

We report a molecular beam epitaxy strategy to achieve a low density of O-band electrically tunable InAs/InGaAs quantum dots (QDs) on GaAs(001) substrates. Our approach is based on a gradient deposition of InAs in the sub-monolayer regime and subsequent capping with an $In_{0.29}Ga_{0.71}As$ strain-reducing layer to redshift the emission wavelength. For different growth conditions, we investigate the optical properties of the dots using photoluminescence mapping and correlate them with structural properties determined by scanning transmission electron microscopy. Using a surface roughness modulation technique and synchronizing InAs sub-monolayer deposition cycles with substrate rotation, we control the dot density and position low-density regions ($<10^8$ cm^{-2}) on the substrate. Hyperspectral imaging is used to map the spatial and spectral characteristics of many individual dots in the low-density region, confirming that our approach applies to conventional molecular beam epitaxy growth on (001) surfaces. Finally, we tune the QD emission wavelength within the O-band using electric fields and demonstrate single-photon emission with $g^{(2)}(0) = 0.020 \pm 0.014$.

I. INTRODUCTION

Epitaxial semiconductor quantum dots (QDs) can be employed as efficient single-photon sources (SPSs) required for photonic quantum technologies, such as quantum communication networks and quantum computing.[1–5] The majority of studies have focused on InAs/GaAs quantum dots emitting at wavelengths below 1 μm, whereas fiber-based quantum technologies compatible with existing telecommunication infrastructure require SPSs with high photon indistinguishability and extraction efficiency operating in the telecoms O-band (~1.3 μm) or C-band (~1.55 μm), respectively.[1,6] Efficient SPSs call for the incorporation of QDs into optical cavities for practical applications with high-rate single-photon emission. The well-established technology and fabrication scalability of GaAs-based photonic heterostructures, including electrical control, make them particularly advantageous for photonic quantum technologies.[3,5,7–9] However, simultaneously achieving emission in the telecom bands and a low density of InAs QDs grown on GaAs substrates remains challenging due to the difficulty of growing sufficiently large and In-rich dots.[7,10,11]

The low-temperature emission wavelength of self-assembled InAs/GaAs QDs grown in Stranski–Krastanow (SK) growth mode and the growth temperature range of 480–520 °C do not usually exceed 1.2 μm.[7,12,13] Several approaches have been followed to redshift the emission of InAs QDs grown on GaAs substrates into the telecommunication spectral windows. These include (i) the overgrowth of InAs QDs grown on GaAs by an In(Al,Ga)As(N) layer [the so-called strain-reducing layer (SRL)],[5,7,10,14–16] (ii) embedding InAs QDs grown in asymmetric In(Al,Ga)As quantum wells,[17,18] and (iii) growth of InAs QDs on metamorphic In(Al,Ga)As buffer layers.[19–21] Each of these approaches is based on the possibility of engineering band profiles leading to a redshift of the QD emission through the reduction of the compressive strain of InAs/Ga(In)As QDs and/or band-offset.[7,10,17–21] It has been demonstrated that these approaches can be used for the development of nanophotonic devices with high single-photon emission efficiency,[5,22,23] integration with fiber-optic infrastructure,[9] and the deterministic fabrication of QD-resonator structures.[4,24,25] To develop QD-based SPSs, the first requirement is to achieve control over the fundamental self-assembly process of InAs QDs with low density, allowing for tuning of the QD emission wavelength. Nevertheless, a wafer-scale strategy for epitaxial growth of QDs with low density and certain optical and structural properties is not yet completely realized. This arises from the steep onset of QD nucleation at a critical InAs layer thickness and a complex interrelation of the growth parameters (growth temperature, indium and arsenic flux, deposition time, growth interruption time, and overgrowth rate) that complicates the stable and reproducible formation of QDs with well-defined and uniform properties.

A gradient growth approach based on the intrinsic flux non-uniformity along the substrate surface in molecular beam epitaxy (MBE) provides a flexible way for optimizing both QD and quantum well active regions in optoelectronic devices.[11,13,26–30] In particular, the gradient QD growth approach offers a reliable strategy for controlling the QD surface density and studying the QD optical properties as a function of InAs coverage.[11,13,19,26,28,29,31–33] A comprehensive experimental study of the flux non-uniformity in MBE over stationary and rotating substrates has been conducted by Wasilewski *et al.*[26,27] These authors showed that the layer thickness as a function of the position on the substrate without rotation can change in the range of ±20% along the diameter of a 2-in. wafer.[26,33] The critical InAs coverage of GaAs for the transition from the 2D to the 3D in SK growth mode ranges from 1.6 ML (monolayer) (measured by AFM) to 1.8 ML (measured by RHEED), as has been carefully studied by many groups.[12,28,29,34–36] Despite the gradient growth universality in MBE, which enables control over the QD surface density, achieving reproducible low-density InAs/Ga(In,Al)As QDs with the targeted emission wavelength and desired optical and structural properties demands precise control over the fundamental aspects of the self-organized processes and growth parameters across the entire substrate.[35,37,38]

Here, we report the development of an MBE growth strategy for low-density self-assembled InAs/InGaAs QDs emitting in the O-band, suitable for the fabrication of SPSs. Our growth strategy relies on a gradient deposition of sufficiently large and In-rich InAs QDs grown in the sub-monolayer (ML) regime with a density modulation technique using a GaAs pattern defining layer (PDL)[29] and overgrown by the InGaAs SRL to achieve low-density O-band InAs/InGaAs QDs with modulation of the areal density across the entire substrate. We correlate the gradient deposition of InAs QD ensembles by synchronizing the substrate rotation with the sub-ML deposition and investigate the impact of a growth temperature gradient across the substrate on the QD optical properties. Using the spatial distribution and the spectral emission properties of a large set (>500) of individual InAs/InGaAs dots characterized via hyperspectral imaging (HSI), we confirm that the developed growth strategy is universal and can be utilized for realizing quantum light sources for use in fiber-based quantum networks and integrated quantum photonic systems. Finally, we demonstrate electrical tunability of QD emission in the O-band and correlate results with atomic-scale QD structure and composition elucidated via aberration-corrected scanning transmission electron microscopy (STEM) and energy-dispersive X-ray (EDX) spectroscopy.

II. EXPERIMENT

The InAs/Ga(In)As QD heterostructures were grown on undoped 2-in. GaAs(001) substrates using a Veeco Gen II MBE equipped with conventional effusion cells for group-III elements and a valved cracker cell for arsenic. All samples contain a buffer layer, 30 periods of a short-period AlAs (2 nm)/GaAs (2 nm) superlattice, followed by a 50–150 nm GaAs layer grown at a substrate temperature (T_S) of 600 °C, measured by a calibrated infrared IRCON pyrometer. Primarily, we used an As_4 beam equivalent pressure P_{As}(BEP) of 1×10^{-5} Torr measured at the substrate position using a Bayard–Alpert ion gauge. Before the InAs deposition, we grew a 15 nm-thick GaAs PDL without rotation at T_S = 580 °C, aligning the Ga-cell toward the secondary flat of the 2-in. GaAs(001) substrate.[29] Directly after the deposition of the PDL, we reduced T_S for the QD growth, followed by a stabilization break. In addition to pyrometer measurements, the QD (T_S) was controlled using reflection high-energy electron diffraction (RHEED) by monitoring the transition of the GaAs surface reconstruction from (2×4)As to $c(4 \times 4)$As under As flux. To grow QDs in SK growth mode, we deposited a gradient of 1.6–2.8 MLs of InAs at the substrate's center in the sub-ML regime with a sequence consisting of an InAs growth time

t_g = 3 s and an As exposure pause time t_p = 3–51 s. The temperature T_S was in the range of 480–550 °C, and the arsenic pressure was P_{As}(BEP) = 0.7 ×10^{-5} Torr. After the QD formation, we reduced T_S by 25–30 °C during a 1–2-min interruption under As supply. Subsequently, the InAs/GaAs QDs or InAs/InGaAs QDs were overgrown by 10-nm-thick GaAs or 7-nm-thick $In_{0.29}Ga_{0.71}As$ SRL and 2-nm-thick GaAs, respectively. After capping the InAs QDs, T_S was linearly increased to 600 °C and P_{As}(BEP) was set back to 1 × 10^{-5} Torr for additional growth of 120–150 nm GaAs or $Al_{0.33}Ga_{0.67}As$ layers. Growth rates of GaAs, AlAs, and InAs were 2.00 ± 0.02, 1.00 ± 0.01, and 0.150 ± 0.003 Å/s, respectively. The indium cell temperature remained constant during the InAs QDs and $In_{0.29}Ga_{0.71}As$ SRL growth.

Figure 1 shows a schematic representation of the effusion cell position in the horizontal MBE growth chamber and the initial orientation of the substrate before the deposition of the GaAs PDL and the InAs/GaAs QDs. The standard dual filament effusion cell (C4 in Fig. 1) with a conical pyrolytic boron nitride (PBN) crucible (cone angle $\beta \approx 4°$) was used for gallium. The single filament indium effusion cell (C6 in Fig. 1) had a conical PBN crucible with $\beta \approx 8°$.

Photoluminescence mapping measurements were carried out using an experimental setup based on a He-flow cryostat under continuous wave (CW) non-resonant laser excitation with a wavelength of 660 nm. The excitation power density was varied in the range ρ_{exc} up to 0.3 W/cm^2 with a spot diameter on the sample of ~0.3 mm. The luminescence was recorded using a spectrometer equipped with an InGaAs linear array detector. In these measurements, the PL mapping area of the 2-in. wafers in the He-flow cryostat is limited to 45 mm in diameter.

Structural measurements of the QDs were performed using atomic force microscopy (AFM) and STEM. Here, a Bruker Dimension Icon system was used to perform AFM measurements in tapping mode, and a Titan Themis 60-300 STEM equipped with an aberration corrector for the probe-forming optics and a ChemiSTEM EDX system was used for structural characterization, operated at 300 kV.

III. RESULTS AND DISCUSSION

A. Gradient growth of InAs QDs on the GaAs substrate

The key features of our developed growth strategy are the implementation of a PDL to modulate the surface roughness on the substrate and optimization of the sub-ML InAs deposition cycle sequence. Specifically, before InAs QD growth, we deposit a 15 nm-thick GaAs PDL without rotation, aligning the Ga-cell toward the secondary flat of the 2-in. GaAs(001) substrate (Step 1, Fig. 1). Immediately after the GaAs PDL deposition, the T_S^{InAs} is ramped down from 580 to 520 °C before subsequent InAs deposition without excessive In desorption and preserving the GaAs PDL surface morphology. Optimization of the sub-ML InAs deposition cycle sequence was carried out considering that QD nucleation in SK growth mode can be described by the "superstress" parameter ϑ, taking into account the case of unintentional In–Ga intermixing on the interface at T_S^{InAs} > 480 °C.[36] This parameter is defined as $\vartheta = (\theta/\theta_{eq} - 1)$, where θ is the coverage, and θ_{eq} is the quasi-equilibrium coverage.[39] Nucleation begins once the wetting layer (WL) reaches a critical coverage θ_{cr}, at which point $\vartheta > 0$. The nucleation stages of the SK growth mode are divided into the following: (1) formation of a wetting layer with θ_{eq}; (2) as the coverage increases beyond θ_{eq}, the layer becomes metastable but insufficient for QD nucleation; (3) when the deposited layer reaches θ_{cr}, the nucleation barrier is minimized, while the nucleation rate is maximized.

The first step of the MBE growth optimization is the selection of the growth temperature T_S. Higher T_S provides an increase in island volume due to the increased adatom diffusion coefficient and weaker influence of diffusion barriers.[12] Based on our RHEED pattern

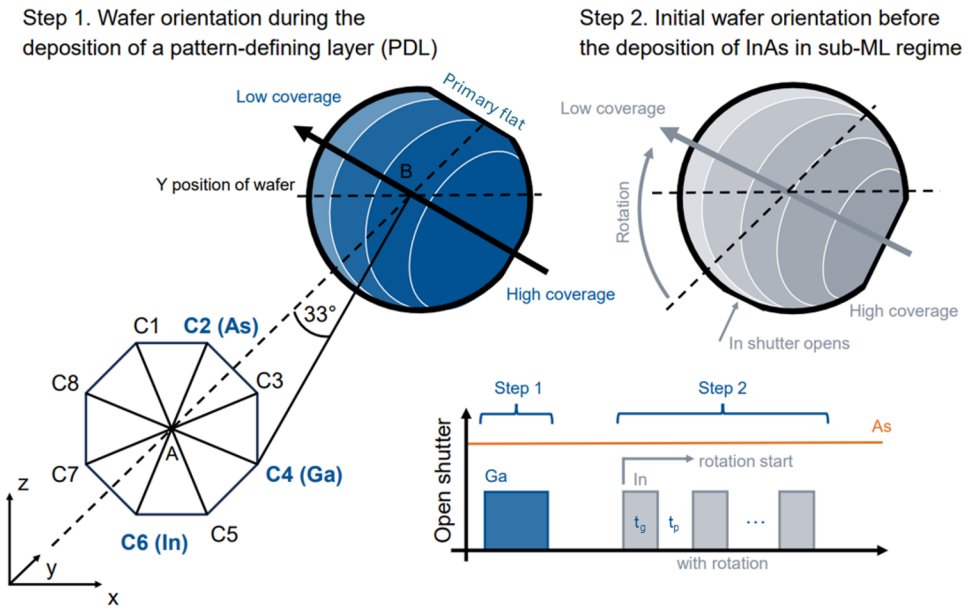

FIG. 1. Schematic of the initial cell-substrate geometry (xy is a horizontal plane) during the deposition of the GaAs PDL at T_S = 580 °C (step 1) and initial orientation of the substrate before deposition of InAs in the sub-ML regime. With t_g and As exposure break time t_p (step 2) at T_S^{InAs}, the shutter sequence for Ga, In, and As cells employed during the PDL growth and the sub-ML InAs deposition cycles are synchronized when $t_g = T/2$ and $t_p = (2N + 1) \cdot t_g$, where T is a substrate rotation period and N is a natural number.

transition from 2D to 3D during InAs/GaAs QD growth at the substrate center with rotation and continuous deposition, the InAs desorption rates are 5×10^{-4} and 2.5×10^{-3} ML/s at T_S = 530 and 540 °C, respectively. To minimize In desorption and maximize the diffusion length of In adatoms, all samples discussed in this paper were grown at T_S = 520–525 °C, with an As P_{As}(BEP) = $7 \times P^{cr}_{As}$(BEP) = 7×10^{-6} Torr, where P^{cr}_{As}(BEP) is the critical value for observing the (2 × 4)As reconstruction on the GaAs(001) surface by RHEED during GaAs growth at T_S = 600 °C with a growth rate of 2.00 ± 0.02 Å/s.

Figure 2 compares the spatial maps of the integrated PL intensity over the range 1000–1400 nm from the InAs/GaAs QDs as a false color representation. These datasets were recorded at room-temperature from the following three samples: (i) a sample grown using standard gradient deposition without rotation and PDL [**S1**, Fig. 2(a)], (ii) samples grown with GaAs PDL and sub-ML InAs deposition without rotation [**S2**, Fig. 2(b)], and (iii) a sample with 45°-step deposition cycles [**S3**, Fig. 2(c)]. All samples were grown at the same T_S^{InAs} = 520 °C and P_{As}(BEP) = 1×10^{-5} Torr. The InAs coverage consistently varied across the substrate, with higher coverage observed near the substrate's primary flat and lower coverage toward the opposite primary flat side by depositing from an inclined In effusion cell. Each map is individually normalized to the integrated PL intensity maximum. These maps reveal the evolution of the PL intensity pattern, transitioning from the standard InAs gradient deposition without a GaAs PDL [Fig. 2(a)] to a stripe pattern with a clear modulation of InAs/GaAs QD emission along the horizontal direction when the GaAs PDL is grown [Figs. 2(b) and 2(c)].

The integrated PL intensity distribution along the coverage gradient exhibits a non-monotonic behavior, reflecting the evolution of the emission properties as a function of the InAs coverage and the corresponding density of InAs/GaAs QDs. Moving from the primary flat toward the top of the substrate, the nominal coverage of InAs presented in Fig. 2(a) ranges linearly from 2.2 MLs (bottom) to 1.57 MLs (top). The PL map in Fig. 2(a) indicates that as the InAs coverage increases, the PL intensity reaches a maximum value within the nominal coverage range of 1.8–2.1 MLs and decreases in regions with coverage below 1.8 MLs (above the substrate center) and above 2.1 MLs (below the substrate center). This behavior is characteristic of the gradient growth mode; the continuous decrease in integrated PL intensity below 1.8 ML reflects a direct reduction in QD density, while the drop in PL intensity above 2.1 ML arises from unfavorable QD ripening into larger islands, which accumulate sufficient elastic energy for plastic relaxation of the InAs islands with non-radiative recombination centers.[7,10,12,40]

Figures 2(b) and 2(c) show PL maps of samples **S2** and **S3** grown with a nominal 15-nm-thick GaAs PDL grown without rotation, aligning the Ga-cell toward the secondary flat (see Fig. 1). In contrast to **S1**, sample **S2** was grown using sub-ML InAs deposition mode with the interruption time t_p = 51 s after each InAs deposition cycle of duration t_g = 3 s. The nominal coverage gradient of sample **S2** ranges linearly from 3.3 MLs (bottom) to 2.4 MLs (top) in the vertical direction, as shown in Fig. 2(b). Implementing sub-ML InAs deposition with the long t_p on stationary substrates together with the GaAs PDL drastically modifies the PL map pattern. In addition to the expected PL intensity modulation with a horizontal spatial periodicity of ~2 mm induced by the PDL,[29] Fig. 2(b)

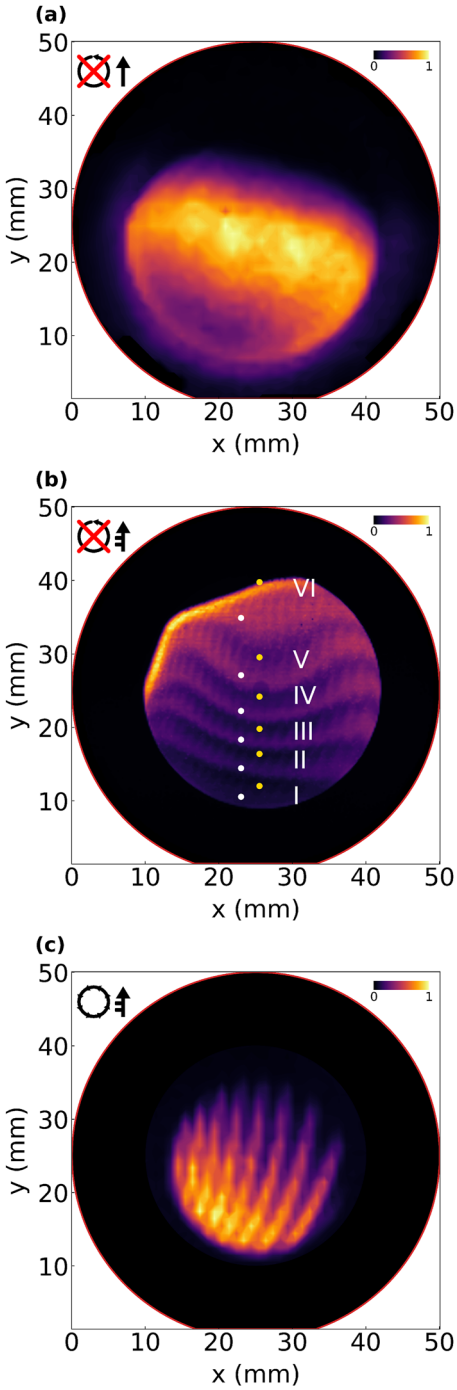

FIG. 2. (a)–(c) False color maps of the integrated PL intensity from the InAs/GaAs QDs acquired at RT from the 2-in. GaAs(001) substrates. (a) Sample **S1** is grown using standard gradient deposition for 40 s without rotation, or a PDL. Samples **S2** (b) and **S3** (c) are grown with a nominal 15-nm-thick GaAs PDL and a sub-ML InAs deposition. **S2** is grown without rotation by depositing 19 InAs cycles, each consisting of 3 s of growth followed by a 51 s break. **S3** is grown by depositing 12 InAs cycles, each consisting of 3 s of growth followed by a 5 s break, with the first 4 cycles without rotation, aligning the In-cell to the primary flat, while the remaining eight cycles use 45° step rotation.

reveals a pronounced PL intensity modulation in the vertical direction.

The growth of the Ga(In,Al)As PDL before the formation of the QDs can be used as a method to control the local dot density on the substrate.[11,29,31] The PDL grown without rotation in the layer-by-layer regime results in a surface roughness modulation across the entire substrate, consisting of fully and partially completed monolayers. This morphology is characterized by the presence of monolayer islands and atomic steps.[26,29] The atomic step density in the so-called rough region varies between ~11–12 μm^{-2}, whereas the regions classified as flat exhibit a much lower step density of about 3–5 μm^{-2} (see Ref. 29). When stress-driven nucleation is taken into account, the presence of the PDL increases local surface roughness, causing a preferential nucleation of InAs islands in the rough regions compared to the flat due to the modification of the formation energy and decreases the nucleation barrier [free energy of island formation $\Delta G(rough) < \Delta G(flat)$].[39] This modification allows QD nucleation in the presence of surface steps to occur within the coverage interval $\theta_{eq} \leq \theta < \theta_{cr}$. As a result, the QD density in rough regions is typically at least one order of magnitude higher than in flat regions.[29] This spatial QD density modulation leads to PL intensity modulation with horizontal periodicity observed in Figs. 2(b) and 2(c).

The continuous decrease in the integrated PL intensity with increasing InAs coverage from top to bottom in Fig. 2(b) confirms the trend observed in Fig. 2(a). Despite this overall decrease, a distinct alternating intensity pattern consisting of downward-curved regions extending from bottom to top is visible in Fig. 2(b). We attribute this behavior to the formation of QD generation boundaries associated with the sequential nucleation of multiple QD generations once the local InAs coverage exceeds the critical value θ_{cr}.[41] Pairs of white and yellow markers indicate representative areas corresponding to individual QD generations, labeled I–VI. In the sub-ML deposition mode without substrate rotation, each cycle consists of an InAs deposition of $\theta(t_g) = 0.15$ ML followed by an interruption time of $t_p = 17 \cdot t_g$. Since the QD nucleation occurs at $\theta_{cr} \approx 1.6$ ML,[34,35] the initial deposition cycles form the WL with a spatial coverage gradient. After 9 out of 19 cycles, $\theta \approx \theta_{cr}$ is first reached near the primary flat of the substrate, indicated by the lowest white marker, leading to the nucleation of the I QD generation. Notably, this I QD generation itself exhibits an internal QD density gradient arising from the spatial θ variation across the substrate, reflected by the decrease in PL intensity when moving from the lowest white marker toward the corresponding yellow marker. During long t_p, when no direct indium flux is supplied, QDs of the I generation can increase in size through metastable adatom accumulation on the WL surface as well as by solid-state diffusion.[39] In the latter case, QD growth occurs at the expense of the WL itself, resulting in a progressively thinner and less strained residual WL. Subsequent sub-ML deposition cycles modify WL and existing QDs, predominantly increasing the size of the existing QDs, which might particularly suppress further nucleation within the yellow-marked region of the I QD generation until a local second critical thickness[7] θ_{cr}^{second} is reached. Simultaneously, the continued sub-ML deposition in regions without QDs [above I generation in Fig. 2(b)] drives the local coverage toward θ_{cr}, initiating the nucleation of a second QD generation. According to this scenario, the boundaries between existing QDs and newly formed QD generations should exhibit not only PL intensity alternatingly associated with changes in QD density but also modifications in the size of existing QDs from earlier generations. These size variations are expected to correlate with the ground-state emission energy, in good agreement with the ground-state PL emission analysis presented in Sec. III B (see Fig. 5).

The spacing between these fronts can be tuned by adjusting the deposition cycle duration. The downward curvature of the transition fronts observed in Fig. 2(b) is attributed to heat-sinking effects in the MBE system, which induce a radial temperature gradient across the substrate.[37] This temperature variation shifts the transition fronts toward regions of higher nominal coverage (see Figs. 9 and 11 in the Appendix). As the ratio t_p/t_g in the deposition cycle, $t_{cycle} = t_g + t_p$, increases, a stronger shift of the generation fronts is expected, primarily due to indium desorption at $T_S \geq 520\,^{\circ}C$. Comparing Figs. 2(a) and 2(b), we highlight that PL map features associated with QD generation become clearly visible in the sub-ML deposition regime.

Figure 2(c) presents the PL map of sample **S3**, which was grown by depositing 12 InAs cycles. Each cycle consisted of $t_g = 3$ s of growth followed by $t_p = 5$ s. The first 4 cycles were grown without rotation, aligning the In-cell to the primary flat. The remaining eight cycles employed a 45° step rotation to maximize θ in the central area, while also slightly shifting the maximum overlap toward the primary flat. The nominal θ gradient of sample **S3** ranges linearly from 1.8 ML at the center to 1.5 ML at the edge. The clear PL intensity modulation in Fig. 2(c) is a direct consequence of the roughness modulation in the GaAs PDL.[29]

Substrate rotation during growth improves not only the uniformity of the thickness profile[11,26] but also provides an effective technique to control the InAs coverage θ and QD density in the sub-ML regime, similar to step deposition applied for sample **S3**. Synchronizing the InAs sub-ML deposition times t_g and t_p with the substrate rotation period T enhances both the uniformity and reproducibility of QD growth. Two particular synchronized sub-ML InAs deposition sequences can be defined when $t_g = T/2$ and t_p is $2N \cdot t_g$ for nominally uniform coverage or $(2N+1) \cdot t_g$ for gradient, where N is a natural number. Our method to achieve a θ gradient in this study involves synchronizing $t_p = (2N+1) \cdot t_g$ with $N = 2$ for all further discussed samples. This additionally results in a more convenient nucleation control via RHEED. The influence of the temperature gradient on the PL map pattern for such a gradient is presented in Fig. 11 of the Appendix. We note that a coverage gradient can also be achieved using a more complex sequence of deposition cycles that accounts for the non-uniformity of the In flux due to the specific cell geometry, the relative configuration of the In and As cells, and the temperature gradient on the substrate. For instance, a combination of cycles with and without rotation, along with close to uniform coverage synchronized with rotation, can be applied to control the QD nucleation.[11,29,31] The PL map pattern evolution observed in Fig. 2 shows that the PDL technique can be applied in conventional MBE growth on (001) surfaces regardless of the geometry used in the MBE system. Moreover, it might hold promise to be extended to the epitaxial growth of other materials systems involving strain-driven self-assembly of III–V, II–VI, and group-IV QDs.

B. Structural and optical properties of InAs/Ga(In)As QDs

In the past, a few MBE growth strategies[7,10] have been successfully developed for the growth of heterostructures with InAs QDs overgrown by an In(Ga,Al)As SRL with QD densities below 1 QD per μm^2. These enabled the development of GaAs-based SPSs emitting in the O-band around 1300 nm: using an ultralow InAs growth rate[10] and forming a bimodal distribution with many taller dots.[7] The overgrowth of InAs QDs grown on the GaAs surface by an In(Ga,Al)As SRL with nominal thickness 5–8 nm and In-content 15%–30% results in deeper confinement of charge carriers in the InAs/In(Ga,Al)As QDs due to the complex interplay between increased QD size, changes in the QD aspect ratio, and strain reduction provided by the In(Ga,Al)As capping layer. Typically, the ground state QD emission shift to longer wavelengths does not exceed 150 meV,[7,10,15,17,42,43] which restricts optimizing the MBE growth conditions. Initial InAs QDs with low density overgrown by GaAs should be In-rich and large enough to emit around 1200 nm (1033 meV) at LT. This ensures that the subsequent overgrowth by In(Ga,Al)As will lead to the redshift of the QD emission into the O-band around 1300 nm (954 meV) [see Figs. 3(a) and 3(b)].

Considering these conditions, our developed MBE growth strategy of the InAs/InGaAs QDs has been divided into two parts: (i) InAs coverage control using a shutter-synchronized sub-ML deposition in gradient mode to obtain low-density InAs QDs on the GaAs surface; and (ii) optimization of the overgrowth step with 7-nm-thick $In_{0.29}Ga_{0.71}As$ SRL. While conventional gradient QD growth is a well-established method for controlling QD density,[28] a reduction in InAs coverage is typically accompanied by a blue shift of the ground-state emission at low temperatures (LT) (see Fig. 12 in the Appendix), consistent with earlier studies attributing this behavior to reduced QD size.[38,44] As we show in Fig. 12 of the Appendix, the blue shift of the QD emission in the low coverage region can be overcome using coverage control in shutter synchronized InAs sub-ML deposition mode, which enables precise control of the InAs coverage. All samples discussed in the following were grown using 15 InAs sub-ML cycles synchronized with substrate rotation, with t_g = 3 s and t_p = 15 s times at a rotation speed of 10 RPM.

The subsequent overgrowth of InAs QDs by GaAs or InGaAs SRL inevitably modifies both the QD morphology and In content, accompanied by In–Ga intermixing. Even prior to the capping, nominally pure InAs QDs exhibit a vertical compositional gradient, with the Ga content near the base reaching values exceeding 60%.[45] To suppress additional In–Ga intermixing during overgrowth, we therefore reduced the overgrowth temperature of InAs QDs overgrown with GaAs. Figure 4 shows the evolution of PL spectra for InAs/GaAs QDs overgrown at T_S between 490 °C (top) and 520 °C (bottom). The spectra were acquired in the regions with AFM QD densities as low as 10 QDs/μm^2. A clear trend is observed: increasing the overgrowth temperature reduces the localization energy, typically attributed to either a reduction in QD volume or enhanced In–Ga intermixing.[12] During the capping process, the island height is reduced as the GaAs overlayer is deposited, driving a thermodynamically favorable flattening of the QDs. This process broadens the lateral flanks of the islands[45] and substantially alters the QD aspect ratio, thereby modifying both the effective QD volume and the indium composition. As a consequence, the optical and structural properties of nominally pure InAs QDs are strongly affected. A similar evolution of morphology and composition is expected during overgrowth with an InGaAs SRL. Based on these observations, InAs/GaAs QDs emitting around 1200 nm at LT were first obtained at a reduced substrate temperature of T_S = 490 °C. Subsequent capping with the InGaAs SRL was therefore carried out at the same temperature to minimize In–Ga intermixing. The In flux was kept constant throughout both InAs QD growth and SRL deposition, followed by a 2-nm-thick GaAs cap. After completion of the SRL overgrowth, the T_S was ramped back to 600 °C for continued GaAs growth. The ripening interruption time after the final InAs deposition cycle was fixed at 90 s.

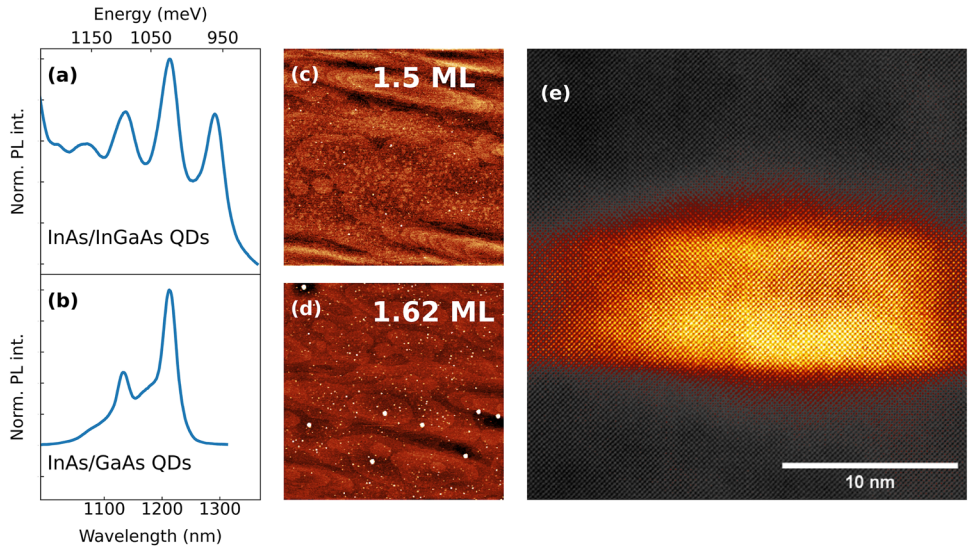

FIG. 3. (a) and (b) Typical ensemble state-filling photoluminescence spectra of InAs/InGaAs and InAs/GaAs QDs measured in the low-density regions at 10 K with an excitation power density of 0.3 W/cm^2, respectively. (c) and (d) 2 × 2 μm^2 AFM images for InAs coverage 1.5 and 1.62 ML along the gradient direction, respectively. (e) False color cross-sectional high-angle annular dark-field scanning transmission electron microscopy (HAADF-STEM) image of a single InAs/InGaAs quantum dot grown at 520 °C and overgrown at 490 °C.

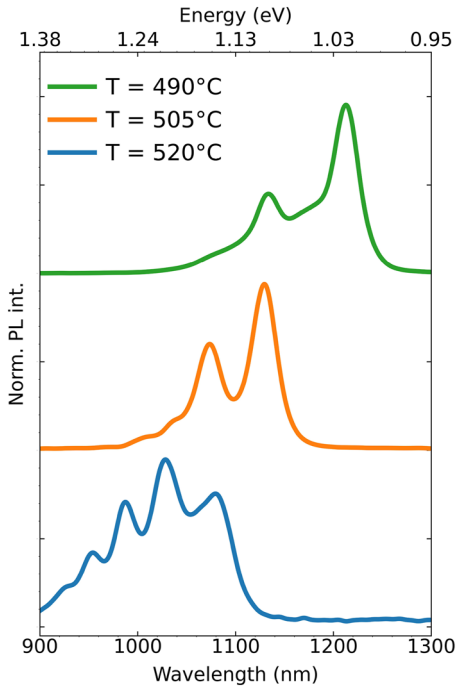

FIG. 4. Normalized PL spectra of InAs/GaAs QDs overgrown at T_S = 490 °C (green), 505 °C (orange), and 520 °C (blue), respectively. All PL spectra are acquired at T = 10 K in the regions where AFM QD density is as low as 10 QDs/μm^2.

A pronounced (around 80 meV) ground-state emission redshift of InAs/InGaAs compared to InAs/GaAs QDs is presented in Figs. 3(a) and 3(b), measured at 10 K with an excitation power density of 0.3 W/cm^2. Figure 3(e) presents a high-angle annular dark-field scanning transmission electron microscopy (HAADF-STEM) image of a representative InAs/InGaAs QD exhibiting a characteristic lens-like morphology. From the HAADF–STEM analysis, the QD aspect ratio H/L, where H denotes the QD height and L the base diameter, is found to be ~0.2. This value is smaller than the aspect ratios of 0.3–0.37 typically obtained from AFM measurements in Fig. 3(d), reflecting the strong modification of the QD shape during capping. As demonstrated in Ref. 43, the excitonic emission redshift in the InAs/InGaAs QD system can reach up to ~160 meV and depends strongly on the final QD shape and In composition, the H/L ratio, and the strain redistribution introduced by the SRL. In particular, the largest redshifts are predicted for aspect ratios close to 0.2, resulting from the combined effects of quantum confinement and the interplay between hydrostatic and deviatoric components of the elastic strain tensor.[43] Based on these calculations, we might estimate that strain-field redistribution contributes ~50–60 meV to the redshift for an InGaAs SRL, while the combined effects of increased QD volume and a reduced H/L aspect ratio account for an additional 30–50 meV. Together, these mechanisms explain the typical QD emission redshift of ~80–100 meV observed in our experiments [see Figs. 3(a) and 3(b)]. To further assess the strain and composition, an aligned series of HAADF-STEM images was used to minimize scan distortions, revealing a strain along the growth direction of ~3%–4% in the InGaAs SRL. By elasticity theory applied to InGaAs/GaAs systems,[46] this translates to In contents of $x = 0.29 \pm 0.03$ within the SRL, which we used to calibrate the HAADF-STEM intensity of the same SRL region. According to Grillo *et al.*,[47] the dependence of the STEM signal on x is approximately linear, from which the average indium content in the interaction volume containing the QD could be derived. Since the QD extension along ⟨100⟩ direction can be assumed isotropic, the extent of the QD along the beam direction is assumed equal to its lateral extension. By measuring the specimen thickness to be 82 nm via comparison of experimental with simulated position-averaged convergent beam electron diffraction patterns, and taking the broadening of the convergent electron beam in the specimen into account, the increase of the HAADF signal in the QD with respect to the SRL could be assigned to a QD with an In content of $x_{min} = 0.41$ and $x_{max} = 0.49$.

We now demonstrate how these findings can be combined to realize MBE growth of low-density O-band quantum dots. Figure 5(a) shows a false-color map of the integrated PL intensity of a fourth sample, denoted **S4**, containing InAs/InGaAs QDs grown at T_S = 520 °C and overgrown at T_S = 490 °C. Figure 5(b) shows the corresponding map of the ground-state emission peak of the

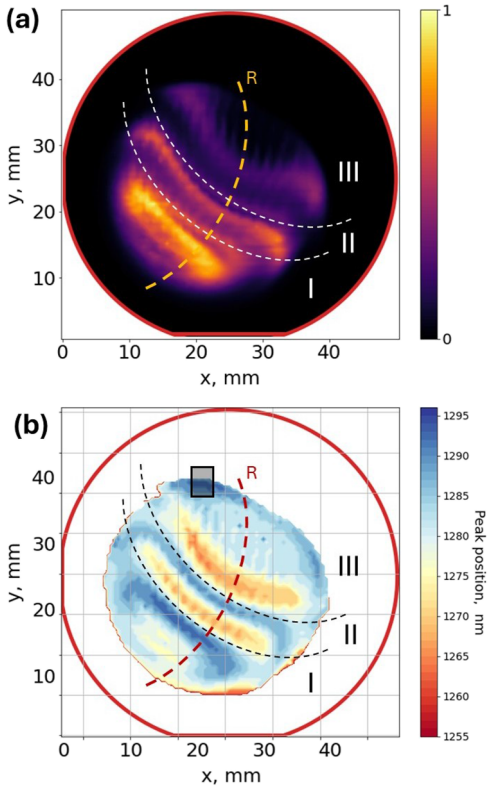

FIG. 5. (a) False color integrated PL intensity map of the sample **S4** with the InAs/InGaAs QDs. (b) InAs/InGaAs QD ground state peak wavelength map. The PL map was measured at 10 K with an excitation power density of 0.3 W/cm^2. The single trajectory along the rough region is highlighted by orange (a) and red (b) lines for clarity.

same sample extracted from PL spectra measured at 10 K. Focusing on the investigation of the structural and optical properties of the InAs/InGaAs QDs grown on the GaAs surface with $\theta < 1.8$ ML (region III in Fig. 5). For AFM measurements of surface QDs, rapid cooling was applied immediately after the completion of the InAs deposition cycles. Figures 3(c) and 3(d) compare AFM images recorded along the gradient thickness in regions corresponding to nominal $\theta \approx 1.5$ and ≈1.62 ML of InAs, respectively. AFM images reveal the presence of two distinct InAs/GaAs dot populations: small and large dots. The small dots have heights ranging from 1 to 5 nm with a base length of around 15–20 nm, while the large dots exhibit heights between 12 and 17 nm and base lengths around 40–45 nm. The combined correlation between the AFM and micro-PL (μPL) imaging indicates that the large dots are responsible for the observed QD PL emission. The density of the large dots decreases as the InAs coverage decreases (see Fig. 13 in the Appendix). Small dots are primarily observed by AFM in the coverage range of 1.45–1.65 MLs, while large dots begin to appear and increase in density, reaching ~10 QDs/μm^2 as the coverage approaches 1.65–1.7 ML. Beyond 1.6 ML, the density of small dots diminishes, while the population of large dots continues to increase [see Fig. 13(d) in the Appendix]. Our AFM data are consistent with the evolution of the densities of both small and large dots as a function of InAs coverage reported by Placidi *et al.*[35] and Bart *et al.*[29] We therefore attribute the progressive suppression of the small-dot population at higher InAs coverage near the 2D–3D transition to the mechanism proposed by Placidi *et al.*,[35] which remains valid in the presence of the PDL. According to the detailed study of surface mass transport in the absence of direct In impingement reported in Ref. 35, the progressive suppression of the small-dot population can be quantitatively explained by kinetic mechanisms. Heterogeneous nucleation of small dots begins at $\theta \approx 1.45$ ML. When the coverage reaches $\theta \approx 1.6$ ML, nucleation of large QDs is initiated. While the average separation distance between the large QDs d remains larger than the cation diffusion length $l = \sqrt{2D\tau}$, QD growth proceeds through the consumption of WL material and available In adatoms. With increasing InAs coverage beyond $\theta > 1.6$ ML, the large dots' density rises rapidly[34] such that $d \leq 2l$. In this regime, all dots gradually evolve into the thermodynamically favorable QD ensemble with similar sizes.[39]

As discussed in Sec. III A, variations in QD size and In composition induced by the presence of the PDL, as well as modifications associated with QD generation formation, are expected to correlate with the ground-state emission energy. QD nucleation proceeds more rapidly in rough regions of the GaAs PDL than on flat regions, as confirmed by the PL intensity modulation observed in samples grown without intentional QD generation formation [see Figs. 2(c) and 14 in the Appendix]. Therefore, we focus here on the PL map analysis of the InAs/InGaAs QD sample **S4**, grown with both PDL and intentionally induced QD generation nucleation. For clarity, one trajectory along a rough region is highlighted by the orange and red dashed lines, while the QD generation boundaries are marked by the white and black dashed lines in Fig. 5. Figure 5(b) shows a slight blueshift of the PL emission along the rough PDL trajectories regardless of the QD generation. This blueshift is clearly observed for QD generations III and II but is less pronounced for generation I. In addition, distinct alternations of the ground-state emission are observed at the transition boundaries between different QD generations, marked by the black dashed lines in Fig. 5(b). All QD generations have a similar emission pattern: within a given generation, an upper region with initially lower QD density generally exhibits redshifted ground-state emission than a lower region of the same generation characterized by higher QD density. This emission pattern is in good agreement with the aforementioned presence of an internal QD density gradient within each QD generation. By comparing the PL patterns of regions I and III, we propose the following scenario: under the selected sub-ML deposition conditions, the I and II QD generations are modified predominantly through the additional incorporation of In supplied by the incoming flux during the formation of subsequent generations. Larger QD sizes consequently lead to a redshift of the ensemble emission within a given QD generation, independent of the local QD density. This effect is reflected in the reduced area of I QD generation with QDs' ground state emitting at wavelengths <1270 nm.

Based on the good agreement between our AFM images and the AFM study of Placidi *et al.*,[35] the slight blueshift observed along the rough PDL trajectories could be qualitatively interpreted within a simple surface mass-transport analysis. Following the study of Heyn[36] and neglecting indium desorption as well as In–Ga intermixing, the total InAs coverage can be written as $\theta = \theta_{WL} + \rho_{QD}\langle V_{QD}\rangle$, where ρ_{QD} is the QD density and $\langle V_{QD}\rangle$ is the average volume of an individual QD. Considering that both the θ and θ_{WL} are similar in neighboring rough and flat regions, the reduced nucleation barrier in the rough regions leads to higher QD density. Consequently, the available indium is distributed among a larger number of QDs, resulting in a smaller average QD volume. As a result, QDs formed in the rough regions are expected to exhibit slightly blueshifted emission.

The combination of the gradient growth approach and synchronized sub-ML deposition developed here provides an additional degree of freedom to control both QD surface density and size. We believe that the modulation of QD optical properties across a single substrate with varying QD density, demonstrated in Fig. 5, could be used not only for the optimization of SPSs but also for QD-based laser heterostructures. Moreover, our developed approach inherently incorporates the previously mentioned bimodal distribution growth modes[7] in regions I and II for achieving long-wavelength emission for individual large QDs, particularly in cases where more than two QD generations are present on the substrate. Large InAs QDs at nominal coverage ~1.6 ML exhibit sizes comparable to those achieved using ultralow InAs growth rates[10] or via bimodal distribution growth modes.[7] In addition, we note that the developed growth approach can be adapted to tailor the emission wavelength of InAs/GaAs QD in the shorter <1200 nm spectral range by employing the so-called indium-flush step.[28,32]

C. Micro-PL spectroscopy of InAs/InGaAs QDs

We continue to validate the results of the AFM and PL mapping experiments in low-density gradient region III of sample **S4**, with a maximum nominal InAs coverage of 1.7 ML, by performing μPL measurements at 4 K. The measurements were carried out using a confocal microscopy setup with CW excitation at 900 nm (above the SRL) and an apochromatic objective with a numerical aperture

of 0.81. The QD emission was detected using a spectrometer with a focal length of 750 mm, equipped with a 1200 lines mm^{-1} grating and an InGaAs linear array detector. The measurements were performed in a region of sample **S4** located in the black area indicated in Fig. 5(b). Figure 6(a) shows the normalized excitation power dependence of the μPL spectra of a representative single InAs/InGaAs QD. The saturation power of the transition labeled CX, emitting at 957.924 meV, is determined to be P_{sat} = 10 μW under 900 nm CW excitation. For the transition lines observed in non-resonantly excited QDs, a typical full width at half maximum (FWHM) of 20–30 μeV (5–7.3 GHz) is extracted. The observed linewidth is limited by the spectral resolution of the μPL setup. The identification of the excitonic states was based on the excitation power dependence of the different charge configurations of the same emitter. The μPL spectrum of an individual InAs/InGaAs QD exhibits a characteristic emission pattern that might be assigned to the neutral exciton (X), biexciton (XX), and charged exciton (CX) transitions. The X and CX show linear dependences of the μPL intensity on the excitation power density, with fitted slopes of 0.95 ± 0.05 and 1 ± 0.05, respectively, while the biexciton (XX) exhibits a quadratic dependence with a slope of 1.9 ± 0.1. To verify the single-photon emission characteristics of the InAs/InGaAs QDs, second-order intensity autocorrelation measurements were performed under CW excitation using the CX transition line. Typical results are presented in Fig. 6(b). A pronounced suppression of multiphoton events at zero time delay, $g^{(2)}(0)$, is observed, confirming the single-photon nature of the emission. From a fit to the autocorrelation data using $g^2(\tau) = 1 - A\exp(-|\tau|/\tau_a)$, we extract a value of $g^{(2)}(0) = 0.020 \pm 0.014$, $A = 0.980 \pm 0.014$, and $\tau_a = 0.75 \pm 0.01$ ns.

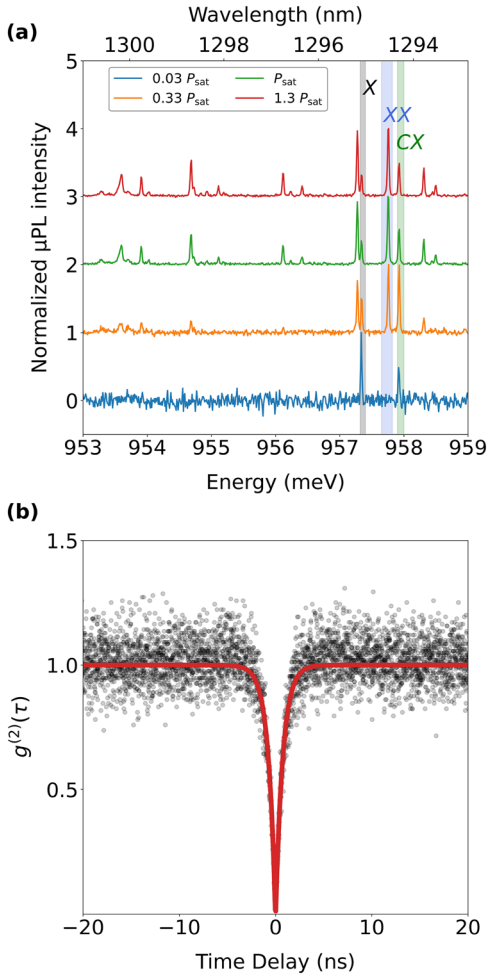

FIG. 6. (a) Normalized excitation power dependence of μPL spectra of a representative single InAs/InGaAs QD measured at 4 K. (b) Second-order autocorrelation measurements of the CX transition lines under CW excitation at 900 nm with a saturation power P_{sat} = 10 μW.

To validate the PDL-induced modification of the QD emission discussed in Sec. III B and to correlate the ensemble emission with the emission properties of individual QDs, we employed μPL scanning hyperspectral imaging (HSI). Following the methodology described in detail by Buchinger *et al.*,[48] HSI was used to characterize and statistically analyze individual InAs/InGaAs QDs in sample **S5**. Sample **S5** was grown under growth conditions similar to those used for sample **S4**. The measurement HSI routine was divided into two parts: a single snapshot image and a hyperspectral imaging scan. An alignment grid was placed on the sample for navigation. The sample was excited with a 730 nm CW laser diode in a closed-cycle cryostat at a base temperature of T = 4 K. In addition, for imaging, the sample surface was illuminated with a 1100 nm LED. Figure 7 presents low-density InAs/InGaAs QD ensemble PL spectra acquired at T = 10 K in nominally flat (F) and rough (R) PDL regions, along with HSI results and subsequent statistical analysis. By correlating the μPL imaging data with the PL map, we have observed that the QD density in regions R2 and F2 does not exceed 0.2 QDs/μm^2, whereas in regions R1 and F1, the average QD density is ~5 QDs/μm^2.

The evolution of the state-filling ensemble PL spectra from F1(R1) to F2(R2) is shown in Figs. 7(a)–7(d). In PL spectra recorded in R1 and F1, the peaks corresponding to the ground-state (s–s) and excited-state (p–p, d–d, f–f) transitions are clearly resolved, reflecting the relative uniformity of the QD ensemble. A comparison between the PL spectra from F1(R1) and F2(R2) reveals the emergence of additional short-wavelength tails, indicating the presence of QDs emitting at shorter wavelengths and a reduced QD ensemble uniformity in the ultralow-density region as low as 0.2 QDs/μm^2. To correlate ensemble PL emission with the emission of individual QDs, the emission wavelength distribution of 505 individual InAs/InGaAs QDs was obtained from six 20 × 20 μm^2 HSI areas in both F2 and R2 regions. As expected, QD ensemble ground-state PL emission peaks in Figs. 7(b) and 7(d) demonstrate a good agreement with histograms measured in regions F2 and R2, corresponding to the most probable emission energy of individual QDs. The peak-emission histogram of 253 QDs measured in region F2 exhibits a maximum near 1310 nm. The histogram of 252 QDs collected in region R2 exhibits a distribution with a peak centered around 1230 nm. We attribute the asymmetry of the peak-emission histogram to two main factors: the presence of smaller QDs and/or QDs with reduced indium composition emitting at wavelengths shorter than the O-band range <1260 nm. The QD emission blueshift observed in R1 and R2 regions with

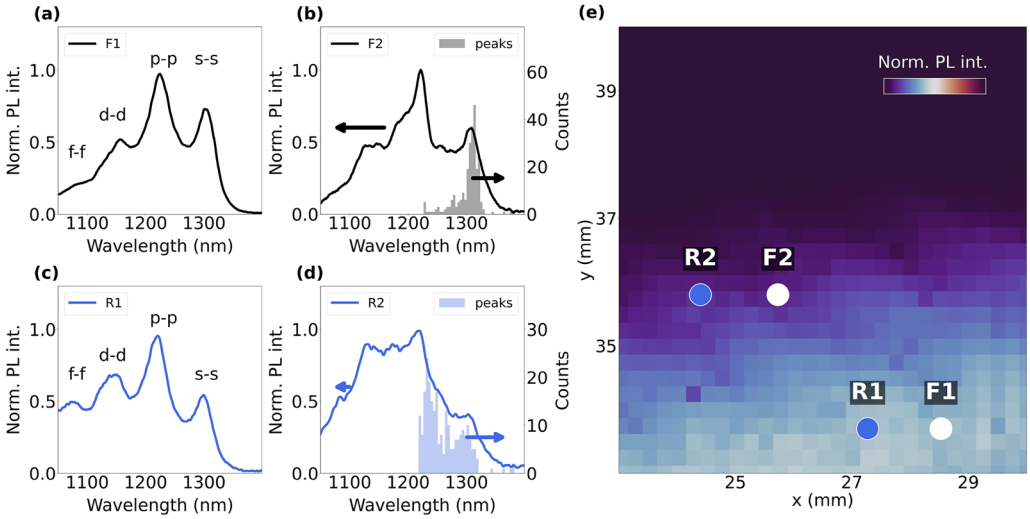

FIG. 7. (a)–(d) PL spectra of the InAs/InGaAs QD ensemble acquired at T = 10 K in regions F1, F2, R1, and R2. (b) and (d) Emission wavelength distributions of 505 individual InAs/InGaAs QDs obtained by HSI measurements in regions F2 (253 QDs) and R2 (252 QDs). (e) PL map of sample **S5** indicating the HSI measurement areas in the rough region R2 and the flat region F2.

increased surface roughness is in good agreement with the ensemble PL peak-emission behavior shown in Fig. 5(b). Our HSI analysis of a large number of individual InAs/InGaAs QDs confirms that the majority of O-band QDs are located in the nominally flat PDL regions, as indicated in Figs. 7(e) and Fig. 5(b). Based on HSI data from the selected area, we estimate that the lateral transition length over which the local QD density decreases from ~5 QDs/μm^2 to below 0.2 QDs/μm^2 is around 3 mm. By extrapolating this estimate to the entire QD-covered substrate area of the samples **S4** and **S5**, we find that the low-density O-band QD area useable for SPSs achieved with the demonstrated MBE growth strategy can reach up to 15%–18% of the total QD-covered area. We believe that the low-density QD area could be further improved by implementing the PDL approach together with uniform synchronization of the InAs deposition cycles and substrate rotation, similar to the strategy described by Kersting *et al.*[11]

D. Electrically tunable device

As demonstrated in previous studies,[1,4,9,16,48,49] the realization of efficient SPSs requires the site-selective fabrication of nanophotonic structures resonant with the QDs. This challenge could be solved using *in situ* photo- or electron-beam lithography or, alternatively, by marker-based PL imaging followed by subsequent lithography steps.[48] To further fine-tune the spectral matching between the QD emission and the cavity mode after fabrication, and thereby enhance the spontaneous emission rate, the quantum-confined Stark effect (QCSE) could be employed.[1,50] Therefore, we focus here on characterizing the QCSE tuning range of O-band InAs/InGaAs QDs, which is relevant for the design of heterostructures with electrical control.[4,9,51] For this purpose, a QD layer of sample **S6**, grown under conditions similar to those used for samples **S4** and **S5**, was embedded within the intrinsic region of an *n*-*i*-Schottky photodiode. The InAs/InGaAs QDs were positioned at the center of a λ-cavity, 35 nm above a 50-nm-thick *n*-GaAs back contact doped to 2×10^{18} cm^{-3}. The active region was followed by a 164-nm-thick GaAs layer, a 40-nm-thick short-period AlAs/GaAs superlattice (3/1 nm) serving as a current-blocking layer, and a 9-nm-thick GaAs cap. The structure also included a bottom DBR consisting of 14 GaAs/AlAs pairs to enhance the photon collection efficiency. Standard semitransparent Ti/Au top and AuGeNi-based bottom contacts were used to electrically gate the photodiode.

Figure 8 demonstrates a typical μPL spectrum of nominally single InAs/InGaAs QDs as a function of applied electric field acquired at T = 4 K in the region where the AFM QD density is as low as 1–2 QDs/μm^2. The various QD emission lines, labeled A–F, redshift with increasing field. For voltages below −1.8 V, no PL signal is observed due to field ionization of excitonic states. As the electric field reduces,

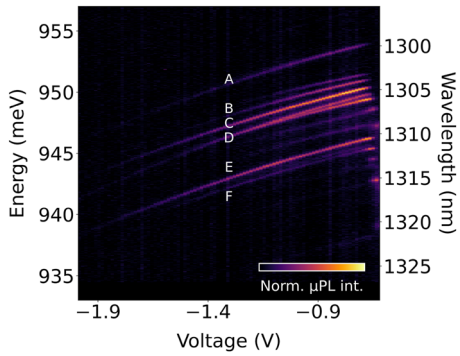

FIG. 8. μPL spectrum of InAs/InGaAs QD (sample **S6**) as a function of applied electric field acquired at T = 4 K in the regions with AFM QD density as low as 1–2 QDs/μm^2 under 900 nm CW non-resonant excitation.

the energy of excitonic states shifts due to the QCSE. The shift is well described by

$$E(F) = E_0 - p \cdot F - \beta \cdot F^2,$$

where E_0 denotes the transition energy in the absence of an external field, p is the static exciton dipole moment, and β is the polarizability.[12,50,52] The electric field **F** is a function of the applied voltage V and the thickness of the region D. It can be expressed as

$$F = \frac{V - V_0}{D}.$$

A parabolic fit to the Stark-shifted A–F lines shown in Fig. 8 demonstrates that p/e for different excitonic complexes ranges from 0.3 to 0.4 nm, while β ranges from 0.6 to 0.7 μeV kV^{-2} cm^2. These value ranges were confirmed by bias-dependent μPL measurements performed across five diodes of sample **S6** and eight individual QDs. The quantity p can be interpreted as a spatial separation between the centers of the electron and hole envelope wave functions in the absence of an external electric field, arising from the spatial gradient of In composition within the QD. Typically, due to the strain profile of the QD, the indium concentration increases from the base toward the apex and from the lateral flanks toward the dot center.[45] As a result, the hole wave function is preferentially situated in the indium-rich upper region, whereas the less localized electron is positioned closer to the dot center.[50] The positive sign of the p observed at $F = 0$ kV/cm supports this interpretation for the InAs/InGaAs QDs grown and studied in this study. Our extracted p values for the O-band InAs/InGaAs QDs are approximately a factor of two smaller than the typical values reported for In(Ga)As/GaAs QDs grown without a flush step.[12,50] This may further indicate that the SRL capping performed at $T_S = 490\,^{\circ}$C partially suppresses In–Ga intermixing and strain-driven In migration away from the QDs. As a result, the effective carrier confinement is stronger than would be expected solely from the increased QD volume. The parameter β is particularly sensitive to the dot height. In the vertical direction, β increases rapidly with QD height,[53] approximately following a quantum well-like scaling of $\beta \propto h_z^4$. Taking typical QD heights of $h^{QD}_{1300\,nm} = 5$–6 nm and $h^{QD}_{930\,nm} = 2.5$–3 nm, the expected polarizability ratio can be estimated as $\beta_{1300\,nm}/\beta_{930\,nm} \approx 7$–$16$. The experimentally observed polarizability of In(Ga)As/GaAs QDs, as carefully studied by many authors,[12,50] typically ranges from 0.1 to 0.4 μeV kV^{-2} cm^2. These values are ~1.5 to 7 times smaller than the polarizabilities obtained for the InAs/InGaAs QDs investigated in this study. Consequently, InAs/InGaAs QDs exhibit a stronger parabolic Stark shift under an applied electric field than conventional In(Ga)As/GaAs QDs. The combination of deeper exciton localization up to 550 meV relative to GaAs, a p/e compared with InAs/GaAs flush QDs, and a large polarizability, together with the MBE growth approach developed in this study, makes O-band InAs/InGaAs QDs promising candidates for integration into the active region of electrically controlled SPSs and for the development of more complex heterostructures based on QD-molecules emitting in the telecom O-band.[4,51]

IV. CONCLUSION

In summary, we demonstrated an MBE growth strategy for realizing high-quality, low-density O-band InAs/InGaAs QDs on standard GaAs(001) substrates with spatially modulated QD density and emission in the telecom O-band at cryogenic temperatures. By combining sub-ML gradient deposition with an InGaAs SRL, the QD emission wavelength was effectively extended while maintaining controlled QD density. Synchronizing substrate rotation with sub-ML InAs deposition, together with surface roughness modulation, enabled spatial control of the QD density and the formation of regions with densities below 10^8 cm^{-2}. PL mapping and HSI were shown to provide a powerful combination for optimizing and controlling the MBE growth of InAs/Ga(In)As QDs. Atomic-scale structure and composition were further clarified by aberration-corrected STEM and EDX spectroscopy. We demonstrate single-photon emission from O-band InAs/InGaAs QDs under CW excitation using the CX transition, obtaining $g^{(2)}(0) = 0.020 \pm 0.014$. These results show that the developed growth strategy could be readily implemented in conventional MBE systems on (001) surfaces and might provide a promising route toward electrically tunable single-photon and entangled-photon devices for quantum photonic applications.

ACKNOWLEDGMENTS

We acknowledge Beatrice Costa from the Technical University of Munich for her assistance in setting up the optical setup. We acknowledge F. Dushimineza from the Ludwig-Maximilians-Universität for assistance in HAADF-STEM measurements. We gratefully acknowledge the Deutsche Forschungsgemeinschaft (DFG) via Project Nos. DIP (FI 947/6-1), MU4215/4-1 (CNLG), INST 95/1220-1 (MQCL), and INST 95/1654-1 (PQET); Germany's Excellence Strategy (Grant Nos. MCQST, EXC-2111, and 390814868); as well as the Bavarian Ministry of Economic Affairs (StMWi) via Project No. 6GQT and Munich Quantum Valley via NeQuS. In addition, we gratefully acknowledge the German Federal Ministry of Research, Technology and Space (BMFTR) via the projects PhotonQ (Grant Nos. FKZ 13N15760 and 13N15759), QR. N (Grant Nos. FKZ 16KIS2197 and 16KIS2209), and 6G-life. A.L. acknowledges support from the BMFTR funded Project Nos. QTRAIN 13N17328, EQSOTIC 16KIS2061, and QR.N 16KIS2200, and the DFG funded Project No. EXC ML4Q LU 2004/1. T.H.-L. acknowledges funding from the BMFTR via Qecs (Project No. FKZ 13N16272). A.T.P. acknowledges funding from the BMFRT via Ferro35 (Grant No. FKZ 13N17641). K.M.-C. acknowledges funding from the Grant No. DFG MU3660/4-1 and funding from the European Research Council within the Horizon Europe innovation funding program under Grant Agreement No. 101118656 (ERC Synergy Project No. 4D-BioSTEM).

AUTHOR DECLARATIONS

Conflict of Interest

The authors have no conflicts to disclose.

Author Contributions

Pavel S. Avdienko: Conceptualization (lead); Data curation (lead); Formal analysis (lead); Investigation (lead); Methodology (lead); Validation (lead); Visualization (lead); Writing – original draft

(lead). **Lukas Hanschke**: Conceptualization (supporting); Investigation (supporting); Methodology (supporting); Supervision (equal); Validation (equal); Writing – review & editing (supporting). **Quirin Buchinger**: Conceptualization (supporting); Formal analysis (supporting); Investigation (equal); Methodology (equal); Validation (supporting); Visualization (supporting). **Nikolai Bart**: Conceptualization (supporting); Methodology (supporting); Software (supporting). **Hubert Riedl**: Investigation (supporting). **Bianca Scaparra**: Investigation (supporting). **Yu Xia**: Investigation (equal); Methodology (equal); Visualization (supporting). **Ziria Herdegen**: Investigation (supporting); Methodology (supporting); Visualization (supporting). **Knut Müller-Caspary**: Conceptualization (supporting); Funding acquisition (supporting); Investigation (supporting); Methodology (equal); Validation (equal); Visualization (supporting). **Gregor Koblmüller**: Conceptualization (supporting); Methodology (supporting); Project administration (supporting); Validation (supporting). **Tobias Huber-Loyola**: Conceptualization (equal); Data curation (supporting); Funding acquisition (supporting); Investigation (supporting); Methodology (supporting); Project administration (supporting); Resources (supporting); Supervision (supporting); Validation (supporting); Writing – review & editing (supporting). **Arne Ludwig**: Conceptualization (equal); Funding acquisition (supporting); Methodology (equal); Resources (supporting); Supervision (supporting); Validation (equal); Visualization (supporting); Writing – review & editing (equal). **Andreas Pfenning**: Conceptualization (equal); Funding acquisition (supporting); Investigation (supporting); Methodology (supporting); Project administration (equal); Resources (supporting); Supervision (supporting); Validation (equal); Writing – review & editing (equal). **Sven Höfling**: Conceptualization (equal); Data curation (supporting); Funding acquisition (lead); Investigation (supporting); Methodology (supporting); Project administration (lead); Resources (equal); Supervision (lead); Validation (supporting); Writing – review & editing (supporting). **Kai Müller**: Conceptualization (equal); Formal analysis (lead); Methodology (supporting); Project administration (equal); Resources (equal); Validation (lead). **Jonathan J. Finley**: Conceptualization (lead); Formal analysis (equal); Funding acquisition (lead); Investigation (equal); Methodology (equal); Project administration (lead); Resources (lead); Supervision (lead); Validation (lead); Visualization (equal); Writing – review & editing (equal).

DATA AVAILABILITY

The data that support the findings of this study are available from the corresponding author upon reasonable request.

APPENDIX: GRADIENT GROWTH OF InAs/InGaAs QDs AND CORRELATION OF STRUCTURAL AND OPTICAL PROPERTIES

The substrate temperature value is a critical process parameter in MBE growth. The temperature gradient across a wafer can lead to significant variations in the structural and optical properties of heterostructures grown by MBE. However, accurately measuring growth temperatures is not easy and depends on the equipment used

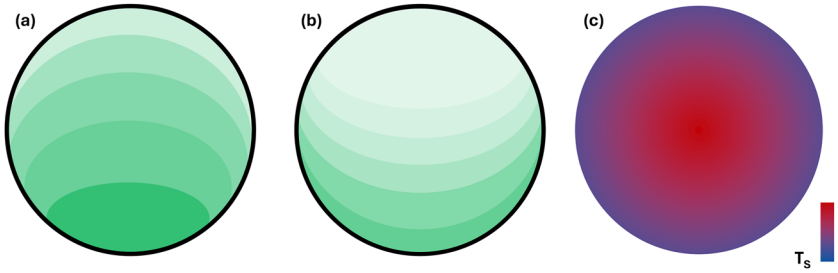

FIG. 9. Schematic of substrate coverage without (a) and with (b) a temperature gradient. (c) Schematic illustration of the substrate temperature gradient.

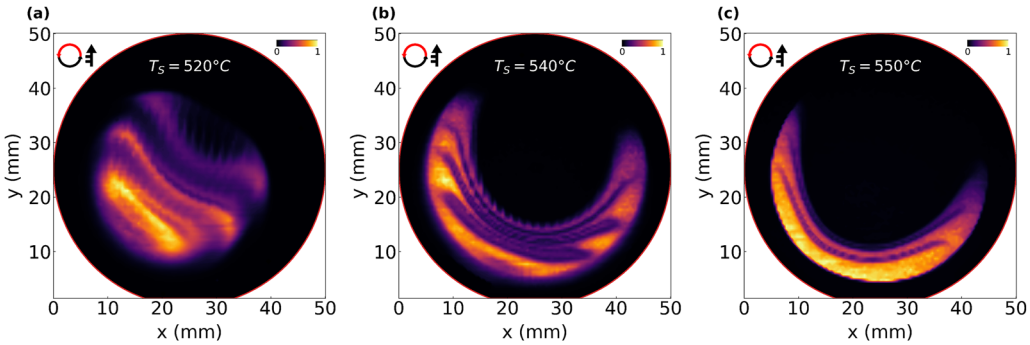

FIG. 10. False color integral PL maps of the InAs/InGaAs QD emission acquired at RT from the 2-inch GaAs(001) wafers. The rotation of samples and InAs sub-ML deposition were initiated simultaneously. All samples shown were grown by aligning the In-cell toward −30° relative to the primary flat. Each cycle consisted of t_g = 3 s followed by t_p = 15 s break at 10 RPM. (a) Sample is grown by depositing 15 InAs at T_S = 520 °C, while (b) and (c) are grown by depositing 17 cycles at T_S = 540 and 550 °C, respectively.

in certain MBE setups. Moreover, accurately measuring the temperature gradient is more complicated and is mostly determined by the heater and substrate holder design. PL mapping is a powerful tool for optimizing a growth process, especially for the gradient growth mode of QDs or QWs.

In our MBE system, the substrate temperature is determined using a calibrated optical pyrometer, which records the temperature from the central region of the substrates. Based on a PL map analysis of samples **S1** and **S2** and a simulation of the InAs coverage on the substrate surface grown without rotation, we find that

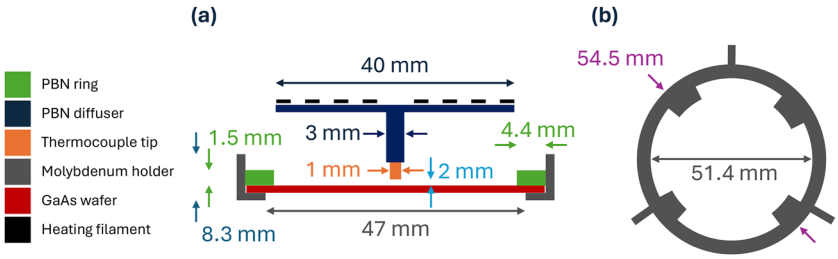

FIG. 11. (a) Schematic cross-sectional view of a manipulator with a GaAs substrate placed on the holder ledge and fixed using the backing PBN ring in the employed MBE system. (b) Schematic of the molybdenum holder.

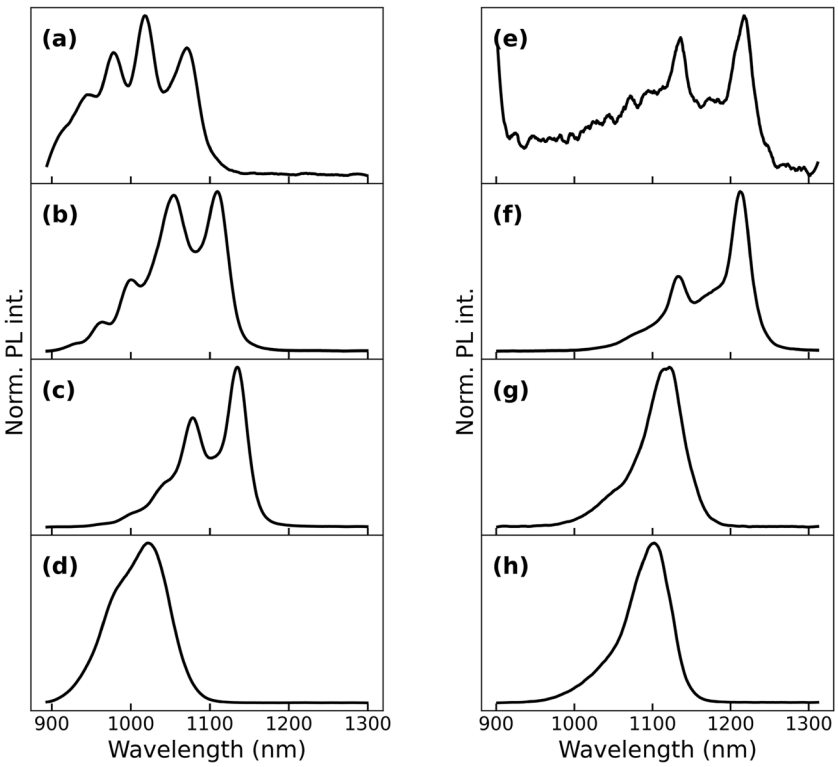

FIG. 12. (a)–(h) PL spectra of InAs/GaAs QD acquired at T = 10 K and an excitation power density of 0.3 W/cm^2 are shown along the InAs coverage gradient: (a)–(d) created using InAs sub-ML deposition without substrate rotation and (e)–(h) gradient depositions with synchronized substrate rotation and sub-ML deposition. Both samples were grown by depositing 12 InAs cycles at T_S = 520 °C and P_{As}(BEP) = 7×10^{-6} Torr. Each cycle includes t_g = 3 s followed by t_p = 15 s. The arrow schematically shows the direction from high to low InAs coverage.

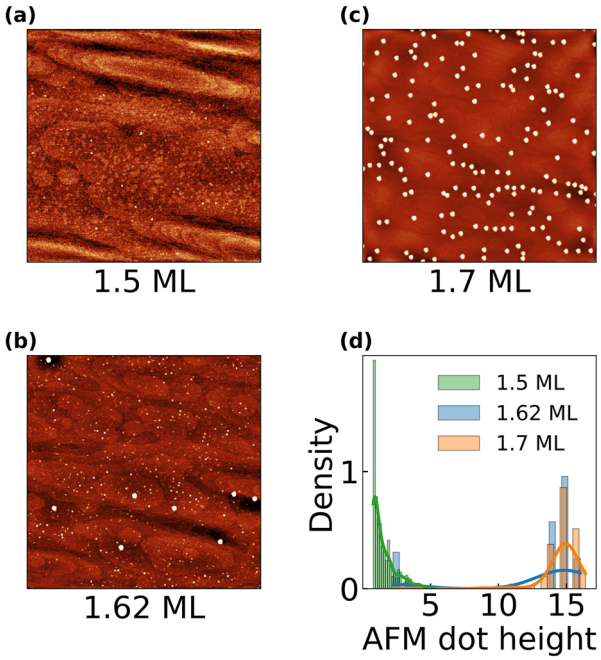

FIG. 13. (a)–(c) $2 \times 2\ \mu m^2$ AFM images for InAs coverage with GaAs PDL $\theta \sim 1.5$, 1.62, and 1.7 ML along the gradient direction, respectively. (d) The kernel density histogram represents the estimation of the probability density function of the height of InAs QDs for the given coverage regions.

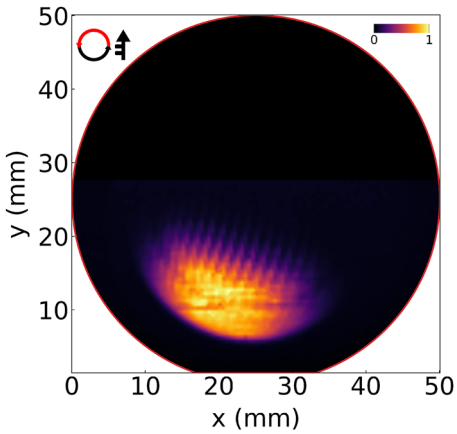

FIG. 14. PL spectra of InAs/GaAs QDs acquired at T = 10 K and excitation power density of 0.3 W/cm^2 are shown along the InAs coverage gradient. The sample was grown by depositing 12 InAs cycles, each consisting of 3 s of growth followed by a 6 s pause, with the first six cycles without rotation, aligning the In-cell to the primary flat, while the remaining six cycles had rotation at 10 RPM.

the region of reliable temperature is limited to the inner diameter of around 4 cm of the 2-in. substrate. Therefore, all further optimization steps and data analysis were carried out with this limitation of the temperature gradient in mind. The molybdenum wafer holder is typically up to 25 °C hotter than the GaAs wafer once the system

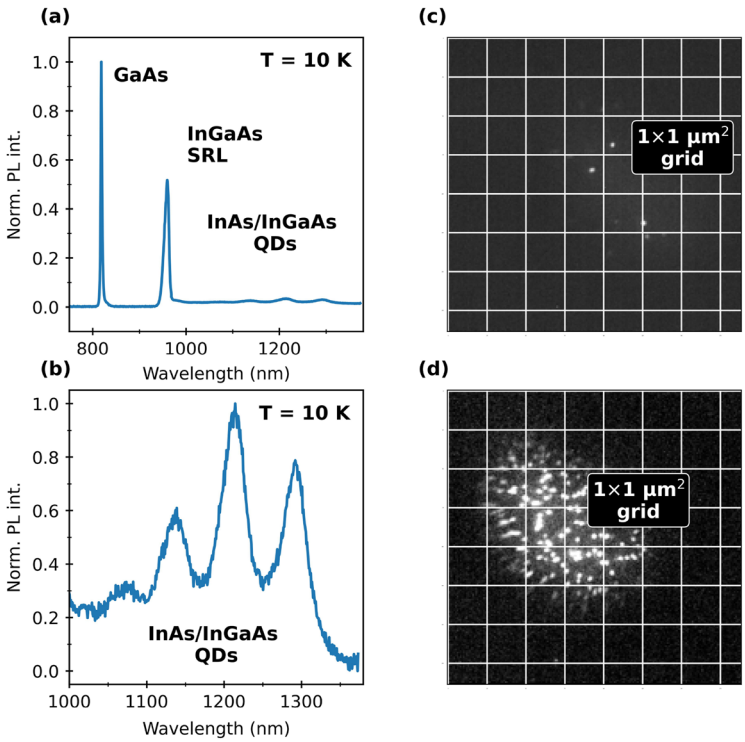

FIG. 15. (a) Typical PL spectrum of sample **S5** acquired region with AFM QD density around 5 QDs/μm^2 at T = 10 K with an excitation power density of 0.3 W/cm^2. (b) The magnification of the region with InAs/InGaAs QDs emission. (c) and (d) Examples of μPL images from single InAs/InGaAs QDs along the density gradient measured without a navigation grid on the sample surface using LED illumination. The spatial distance between the regions where images are acquired is 3 mm.

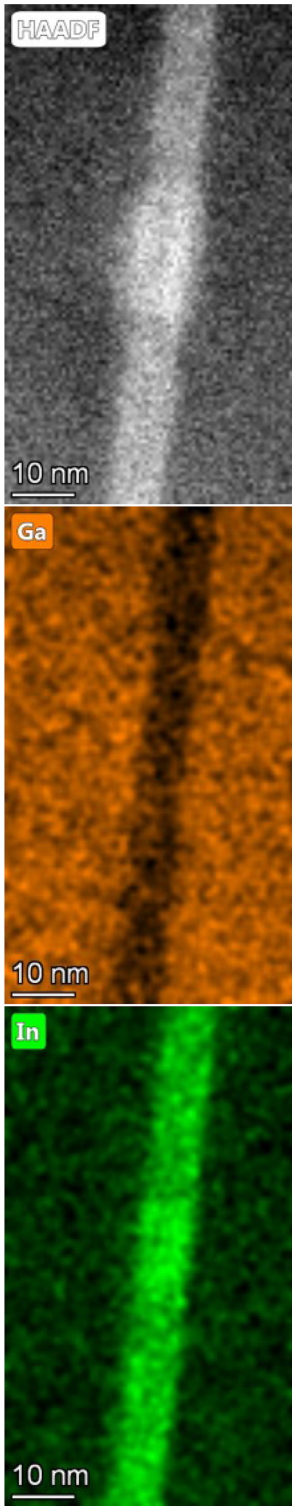

FIG. 16. High-angle annular dark-field (HAADF) and energy dispersive X-ray (EDX) mapping of elemental composition across the InAs/InGaAs QD layer, highlighting Ga and In distribution.

TABLE I. Voigt fit summary for multiple spectral regions and excitation powers.

Fraction of P_{sat}^{CX}	Excitonic state	FWHM (μeV)
0.03	CX	27.0
0.03	X	22.3
0.33	XX	25.8
0.33	CX	26.2
0.33	X	23.4
1	XX	27.9
1	CX	27.2
1	X	24.2
1.3	XX	28.0
1.3	CX	27.4
1.3	X	24.3

stabilizes at the growth temperature. Consequently, an additional heating of the substrate edges occurs from the holder through contact at the ledge.[54] However, it should be emphasized that when the diameter of the heater is smaller than the substrate (see Fig. 11), the wafer edges can be 30–40 °C cooler, reducing the reliable temperature of the inner substrate diameter (see Figs. 9 and 10). The exact temperature distribution is influenced by the complex thermal coupling among the substrate, backing rings, platen, and manipulator heater, which is specific to the configuration of the employed system. As shown in Ref. 37, the temperature profile of the substrate may impact the structural and optical properties of the low-density InAs/GaAs QDs, depending on the location of the low-density QD region during nucleation, ripening, and overgrowth.

Figure 11 shows an evolution of the PL map pattern of InAs/InGaAs QDs grown at different T_S and the same synchronization parameters t_g = T/2 = 3 s and t_p = 5 × T/2 = 15 s.

A PL spectra analysis of the samples grown using a conventional gradient deposition without substrate rotation is presented in Fig. 12. Figure 15 shows broad-range PL spectra of sample S5, with magnified views of the QD emission range in panels [(a) and (b)], together with representative μPL images of individual InAs/InGaAs QDs along the density gradient [(c) and (d)]. Figure 16 demonstrates the HAADF-STEM image and EDX mapping of elemental composition across the InAs/InGaAs QD layer, highlighting Ga and In distribution. Table I summarizes the Voigt fitting results for multiple spectral regions and excitation powers.

REFERENCES

[1] P. Senellart *et al.*, Nat. Nanotechnol. **12**, 1026–1039 (2017).
[2] T. D. Ladd *et al.*, Nature **464**(7285), 45–53 (2010).
[3] J. Wang *et al.*, Nat. Photonics **14**(5), 273–284 (2020).
[4] J. Schall *et al.*, Adv. Quantum Technol. **4**, 2100002 (2021).
[5] M. Albrechtsen *et al.*, Nat. Nanotechnol. **21**, 642 (2026).
[6] N. Tomm *et al.*, Nat. Nanotechnol. **16**(4), 399–403 (2021).
[7] M. Ward *et al.*, Appl. Phys. Lett. **86**(20), 201111 (2005).
[8] A. Schlehahn *et al.*, APL Photonics **1**, 011301 (2016).

[9] A. Barbiero *et al.*, ACS Photonics **9**(9), 3060–3066 (2022).
[10] B. Alloing *et al.*, Appl. Phys. Lett. **86**(10), 101908 (2005).
[11] E. Kersting *et al.*, Nanomaterials **15**(3), 157 (2025).
[12] M. G. D. Bimberg and N. Ledentsov, *Quantum Dot Heterostructures* (John Wiley Sons, 1999).
[13] A. K. Verma *et al.*, J. Cryst. Growth **592**, 126715 (2022).
[14] T. Kakitsuka *et al.*, Phys. Status Solidi C **4**, 2815–2817 (2003).
[15] M. Paul *et al.*, Appl. Phys. Lett. **106**, 122105 (2015).
[16] M. Strauss *et al.*, Nanotechnology **20**, 505601 (2009).
[17] V. Ustinov *et al.*, Appl. Phys. Lett. **74**, 1157–1160 (1999).
[18] L. Sapienza *et al.*, Phys. Rev. B **88**, 155330 (2013).
[19] B. Scaparra *et al.*, Mater. Quantum Technol. **3**, 035004 (2023).
[20] K. Zeune *et al.*, ACS Photonics **8**(8), 2337–2344 (2021).
[21] P. Wyborsk *et al.*, Phys. Rev. Appl. **20**, 044009 (2023).
[22] Z. Chen *et al.*, Nanoscale Res. Lett. **12**, 378 (2017).
[23] S. Kolatschek *et al.*, Nano Lett. **21**(18), 7740–7745 (2021).
[24] A. Dousse *et al.*, Phys. Rev. Lett. **101**, 267404 (2008).
[25] A. Nowak *et al.*, Nat. Commun. **5**, 3240 (2014).
[26] Z. R. Wasilewski *et al.*, J. Vac. Sci. Technol. B **9**, 120–131 (1991).
[27] Z. Wasilewski, "MBE growth of THz quantum cascade lasers," in *Molecular Beam Epitaxy: From Research to Mass Production* (Elsevier, 2013), Chap. 28, pp. 631–655.
[28] S. Fafard *et al.*, Phys. Rev. B **59**, 15368 (1999).
[29] N. Bart *et al.*, Nat. Commun. **13**, 1633 (2022).
[30] M. Ściesiek *et al.*, Cryst. Growth Des. **17**(7), 3716–3723 (2017).
[31] H.-G. Babin *et al.*, J. Cryst. Growth **591**, 126713 (2022).
[32] A. Ludwig *et al.*, J. Cryst. Growth **477**, 193–196 (2017).
[33] A. Rosenauer *et al.*, Phys. Rev. B **64**, 245334 (2001).
[34] D. Leonard, K. Pond, and P. M. Petroff, Phys. Rev. B **50**, 11687 (1994).
[35] E. Placidi *et al.*, J. Phys.: Condens. Matter **19**, 225006 (2007).
[36] C. Heyn, Phys. Rev. B **64**, 165306 (2001).
[37] M. Sharma *et al.*, Sci. Rep. **5**, 15732 (2015).
[38] F. Findeis *et al.*, Physica E **7**, 354–358 (2000).
[39] V. Dubrovskii, *Nucleation Theory and Growth of Nanostructures* (Springer, Berlin, 2014).
[40] P. Frigeri *et al.*, J. Appl. Phys. **102**, 083506 (2007).
[41] N. Bart, "Wafer scale density modulation of self-assembled quantum dots by epitaxial roughness control," Ph. D. thesis, Ruhr-Universität Bochum, Bochum, Germany, 2023.
[42] Y. Yu *et al.*, Nat. Nanotechnol. **18**, 1389–1400 (2023).
[43] A. N. Kosarev and V. V. Chaldyshev, Phys. Rev. Appl. **16**(4), 044046 (2021).
[44] Y. Yu *et al.*, Appl. Phys. Lett. **102**, 201103 (2013).
[45] G. Costantini *et al.*, Phys. Rev. Lett. **96**, 226106 (2006).
[46] K. Müller *et al.*, Phys. Rev. B **84**, 045316 (2011).
[47] V. Grillo *et al.*, Phys. Rev. B **77**, 054103 (2008).
[48] Q. Buchinger *et al.*, Nano Convergence **12**, 36 (2025).
[49] X. Ding *et al.*, Phys. Rev. Lett. **116**, 020401 (2016).
[50] J. Finley *et al.*, Phys. Rev. B **70**, 201308 (2004).
[51] P. Avdienko *et al.*, arXiv:2603.29006 (2026).
[52] A built-in voltage $|V_0| = 0.5$ V was estimated from the onset of current flow under forward bias.
[53] D. A. B. Miller *et al.*, Phys. Rev. Lett. **53**(22), 2173–2176 (1984).
[54] T. J. Rogers *et al.*, J. Cryst. Growth **311**(7), 1676–1679 (2009).